ACS NANO
Cite This: ACS Nano 2018, 12, 2591−2602
www.acsnano.org

ARTICLE

Characterization of Mega-Dalton-Sized Nanoparticles by Superconducting Tunnel Junction Cryodetection Mass Spectrometry

David M. Sipe, Logan D. Plath, Alexander A. Aksenov,† Jonathan S. Feldman,‡ and Mark E. Bier*

Center for Molecular Analysis, Department of Chemistry, Carnegie Mellon University, Pittsburgh, Pennsylvania 15213-2683 United States

ABSTRACT: The characterization of nanomaterials is critical to understand the size/structure-dependent properties of these particles. In this report, a form of heavy ion mass spectrometry, namely, superconducting tunnel junction (STJ) cryodetection mass spectrometry (MS) is used to characterize quantum dot semiconductor nanocrystals and gold nanoparticles. The nanoparticles studied ranged in mass from 200 kDa to >1.5 MDa and included lead sulfide quantum dots, various cadmium selenide and/or telluride-based core−shell quantum dots coated with different ligands, and gold nanoparticles. Nanoparticles were ionized by both matrix-assisted laser desorption ionization (MALDI) and laser desorption ionization (LDI), shot with an aimed ion gun into a flight tube, mass separated by time-of-flight (TOF), and detected by an energy-sensitive STJ cryodetector. STJ cryodetection MS can be used to analyze intact heterogeneous nanoparticles, allowing determination of average particle mass, dispersity, and ligand loading. Some nanoparticles, however, do undergo fragmentation during the MALDI or LDI-TOF mass analyses. The measurement of the energy deposited into the detector was found to be different for different types of particles. Metastable fragments from these nanoparticles were observed at lower energies. The lower energies deposited for metastable fragments can provide insight into the stability and surface compositions of these materials. Cadmium selenide core−shell quantum dots (655 nm emission) conjugated to biomacromolecules, such as cholera toxin B and human serum transferrin, were also analyzed. When compared to unconjugated particles by mass, it was determined that ∼96 cholera toxin B and ∼14 transferrin proteins were attached to the surface of these nanoparticles.

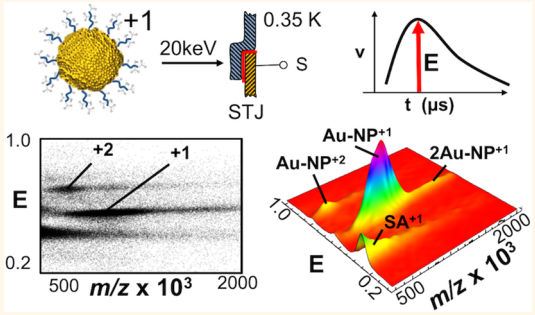

KEYWORDS: *nanoparticle characterization, mass spectrometry, superconducting tunnel junction, heavy ion mass spectrometry, metastable ion, quantum dots, gold nanoparticles*

Nanoparticles (NPs) are defined as a class of materials with one dimension between 1 and 100 nm.[1,2] At the nanometer scale, these particles can exhibit distinct properties related to the onset of quantum effects that are radically different from those of the bulk material.[3,4] Most of these properties are dependent on particle size, but shape and structure also play an important role.[5−7]

One way to classify NPs is based on composition. In this report, we analyzed two classes of NPs: (*i*) metallic and (*ii*) inorganic semiconductor NPs. Metallic NPs are particles with cores composed of metallic elements (*e.g.*, gold, silver, platinum, *etc.*) either of a single element or as alloys. These NPs have optical, electronic, and catalytic properties, which have been used in many different applications. For example, metallic NPs have been used for catalysis, molecular sensing/detection, and managing environmental contaminants.[8−12] These applications utilize metallic NP properties derived from surface plasmon resonance and structural effects.[1,5,12,13] Inorganic semiconductor NPs, sometimes referred to as semiconductor nanocrystals or quantum dots (QDs), are composed of metallic, nonmetallic, or metalloid elements and exhibit photoluminescent properties originating from quantum confinement effects when cluster sizes comprise less than ∼10000 atoms.[14,15] QDs can be synthesized in different sizes and compositions, such as core−shell-type particles, which can be tuned to select emission properties.[4,16,17] Semiconductor nanocrystals have seen application in areas such as photovoltaics and optoelectronics, biomedical imaging and delivery, photocatalysis, and flow cytometry.[18−28]

Characterization of synthetic NPs is essential to understand the interesting size/structure-dependent properties of these particles. Nanomaterials are typically characterized using optical and electron spectroscopy, atomic force microscopy, X-ray crystallography, thermogravimetric analysis (TGA), and more

Received: December 1, 2017
Accepted: February 26, 2018
Published: February 26, 2018

DOI: 10.1021/acsnano.7b08541
ACS Nano 2018, 12, 2591−2602

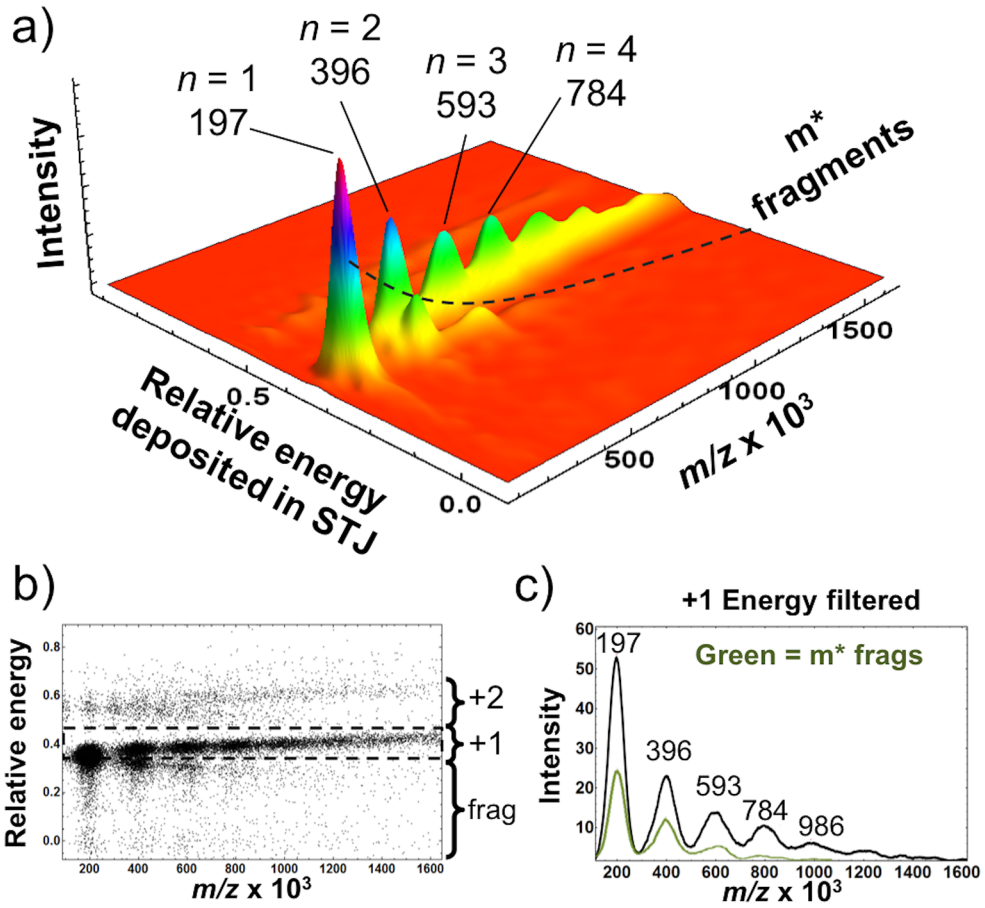

Figure 1. (a) LDI mass spectrum of PbS QDs with a m/z range of 1.0×10^5 to 1.6×10^6. Single QDs were detected at m/z 1.97×10^5 with dimers, trimers, and tetramers at m/z 3.96×10^5, 5.93×10^5, and 7.84×10^5, respectively, up to hexamers at m/z 1.2×10^6. Peak widths increased with increasing mass, as expected. Multimerization of the singly charged QDs is believed to occur during the LDI process. (b) Energy scatterplot mass spectrum of the same data as in (a) with regions of energy for specific charge states indicated. The lower-energy signals beneath singly charged ions indicated metastable fragmentation of the QDs after LDI. (c) Energy-filtered 2D mass spectrum showing data of singly charged intact ions (black trace) and, at lower energies, metastable fragments (green trace); m* = metastable ion.

recently, mass spectrometry (MS).[29−34] All these characterization methods have limitations, due to the physical properties of the NPs, where size, mass, chemical composition, abundance, and stability may all hinder the analysis. MS has typically been employed to study smaller NPs whose molecular weights are <100 kDa and can be detected using conventional instruments;[35−41] however, widespread use of MS for characterizing NPs has been impeded by the complex nature, stability, and ultrahigh masses of these particles. In one study, the analysis of even small, metal nanoclusters (<50 metal atoms) was limited due to the destructive nature of the ionization process used.[42] As a result, the development of "softer" ionization techniques, which allow for intact NP analyses, has been essential to advance MS studies of these complexes. In addition, there is a need for ultrahigh m/z detectors. Conventional mass spectrometers often use ionizing-type detectors with secondary electron emission that is amplified to become the analytical signal. The sensitivity of this technique is dependent on ion impact velocity in order to generate the initial electrons required for observation.[43] As a result, as m/z values increase and ion velocities decrease, the detection response is reduced without the introduction of advanced detection strategies.[44−46]

Although synthetic methods for producing NPs have improved greatly since their inception, with the ability to produce more uniform particles in size and structure, uncontrolled molecular complexity still exists. Most NPs cannot be synthesized with atomic precision; so as a byproduct of synthesis, these particles have a wide distribution of surface ligands and number of core atoms. Small distributions in size lead to large variations in mass, and when coupled with large molecular weights, analysis on conventional mass spectrometers is often not possible. Select mass spectrometers may be able to detect low mass NP ions if the charge states are increased, thus lowering the m/z range required for detection, but higher charge state ions require higher resolving power to gain useful information.[47] Even state-of-the-art high-resolution Fourier transform-based mass spectrometers do not have either the mass range or the resolving power to determine the charge states of mega-Dalton NPs because of the high dispersity of these particles. In addition, even if the NPs were ideally atomically precise, a commercial high-resolution Orbitrap mass spectrometer with a mass range up to m/z 20000 would require 1 mega-Dalton NPs to acquire >50 charges to fall within this m/z range. This high charge state may not be possible even when using electrospray ionization. It should be noted that, recently, researchers modified an Orbitrap mass analyzer to extend the upper m/z limit to ~80000.[48,49]

Superconducting tunnel junction (STJ) cryodetection was first coupled to a time-of-flight (TOF) mass spectrometer in 1996 and has demonstrated near 100% efficiency for detection

DOI: 10.1021/acsnano.7b08541
ACS Nano 2018, 12, 2591−2602

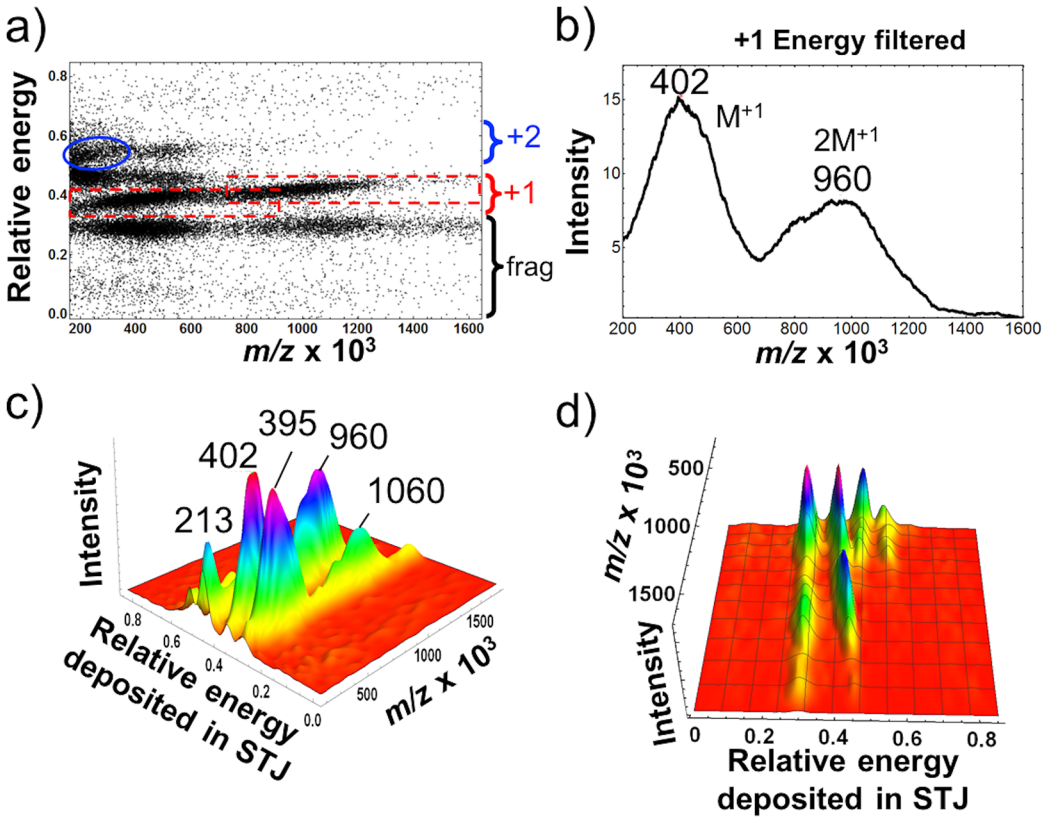

Figure 2. LDI-TOF-STJ mass spectrum of organosol 800 nm emitting core−shell QDs. (a) The energy scatterplot has multiple energy bands, which reflect differences in particle energy associated with ion charge or through energy loss *via* fragmentation. The lower band is assigned to fragmentation from metastable ions originating from singly charged ions. The degree of fragmentation reflects the stability of these NPs after LDI. (b) Energy-filtered 2D mass spectrum showing only singly charged single QDs and dimers (inside red rectangles in (a)). (c,d) 3D mass spectrum of all the points from (a) showing (c) the relative abundance of all peaks and dispersity while (d) shows a rotated view of the energy differences with m/z with more clarity.

of heavy ions at m/z > 100000.[50] The operating principles of STJs have been described elsewhere[51,52] and have been used for the analysis of macromolecules above 100 kDa and exceeding 17 MDa in molecular weight.[53−58] This report demonstrates that STJ cryodetection coupled with laser desorption ionization (LDI) and/or matrix-assisted laser desorption ionization (MALDI) TOF MS provides a useful tool to analyze metallic and inorganic semiconductor NPs. NPs with molecular weights >100 kDa and exceeding 1.5 MDa have been analyzed, whereby average masses and dispersities can readily be determined. Additionally, by measuring deposition energies of the particles impacting the STJ detectors, differences among particle types and metastable fragments have been observed which may aid in the characterization of NP stability and surface structure.

RESULTS AND DISCUSSION

Lead sulfide (PbS) QDs with an infrared (IR) emission wavelength maxima at 1311 nm were analyzed by LDI-TOF-STJ MS. These QDs were coated with a trioctylphosphine oxide (TOPO) shell. Similar PbS QDs have been used in applications related to photovoltaic device constructions.[59] Figure 1a shows the 3D mass spectrum for these QDs and highlights the additional energy dimension available by STJ cryodetection. Without sufficient resolution, the means of cationization (*e.g.*, protonation, anion loss, metal cationization) are unknown, and thus, we represent the charged QDs as $[nM + mX]^{m+}$, where X denotes the mass of a cation. The integer n represents the number of particles associated with the ion, and m represents the number of cations and, in this case, the net charge of the ion. The base peak, $[M + X]^+$ at m/z 1.97 × 10^5 was assigned to singly charged PbS QDs. These QDs appear to be stable in the ion source because under LDI conditions we do not see peak tailing to lower m/z, which is indicative of in-source fragmentation. In addition to the base peak, several singly charged broad peaks were observed at higher m/z values. These peaks have been assigned to nonspecific multimers (n-mers) generated during the LDI process where n > 1. This nonspecific multimeric pattern has been observed previously for LDI-MS of small metal clusters.[60] The dimeric cluster was detected at m/z 3.96 × 10^5, whereas the trimeric and tetrameric species were measured to be m/z 5.93 × 10^5 and 7.84 × 10^5, respectively. Up to hexamers of PbS QDs are readily resolved. The broadness of these NP peaks is due to the dispersity as a result of the QD synthesis. To make this conclusion, we compared the mass spectrum of the protein IgG (see Figure 3 in ref 56) with nearby masses from the PbS QDs. The IgG monomer at 148.3 kDa and trimer at 445.74 kDa had full width at half-maximum (FWHM) values of 5.5 and 11.7 kDa, respectively, whereas the PbS QDs at 197 and 396 kDa had FWHM values that were nearly an order of magnitude higher at 70 and 100 kDa, respectively.

Based on the monomeric mass of 197 kDa, the bulk density of PbS (7.6 g cm^{-1}), and the assumption that TOPO did not contribute significantly to the mass, it was estimated that the PbS QDs had an average diameter of ~4.4 nm. This diameter correlates well with an average core diameter of 4.2 nm

DOI: 10.1021/acsnano.7b08541
ACS Nano 2018, 12, 2591−2602

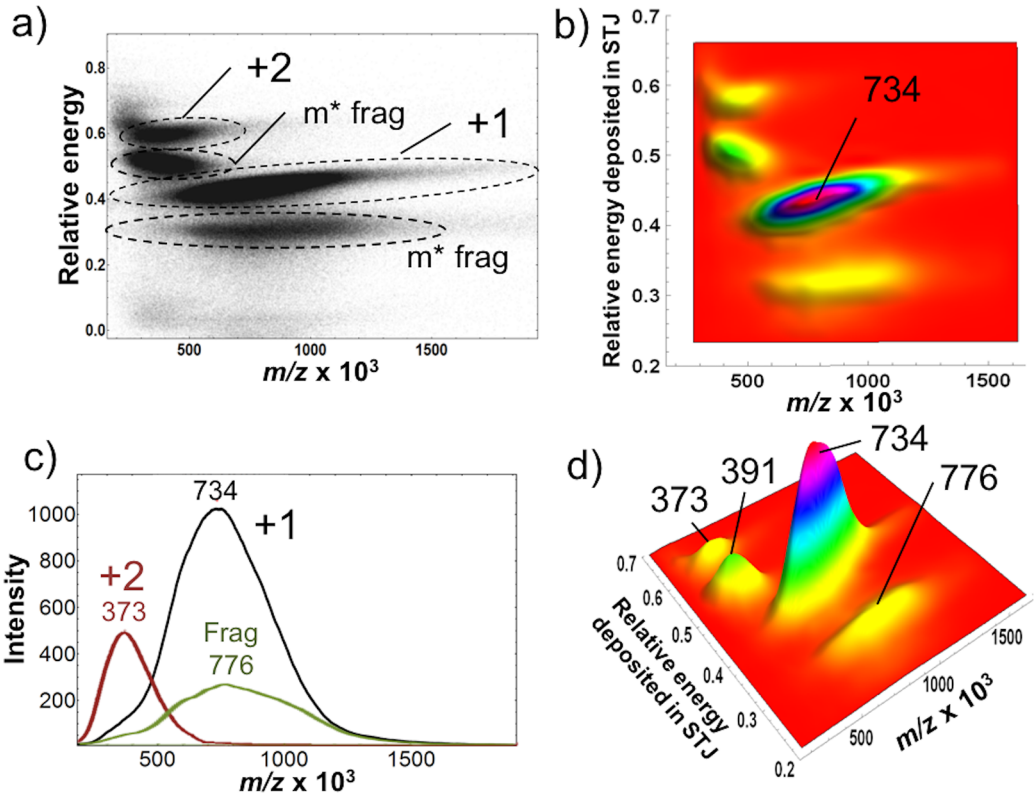

Figure 3. (a) Energy scatterplot generated from the MALDI-TOF-STJ MS analysis of carboxyl-functionalized amphiphilic polymer-coated 800 nm emitting QDs obtained using sinapinic acid as the matrix. Similar to the energy scatterplot of organosol QDs in Figure 2a, there is 25% relative abundance of metastable fragmentation resulting in the signal band immediately below the intact QD bands. (b) Top view of the 3D mass spectrum. Note that the ions appear better separated from those in (a) due to the smaller range of energies plotted. (c) 2D mass spectrum of the intact +1, +2, and metastable fragments from the singly charged precursor ions after energy filtering. (d) 3D mass spectrum of the data in (a) viewed from a different orientation; m* = metastable ion.

provided by the manufacturer[61] using transmission electron microscopy (TEM).

The energy scatterplot LDI mass spectrum of PbS QDs (Figure 1b) shows the relative energies deposited by the impacting particles onto the STJ detector surface *versus* m/z. This plot highlights different energies deposited onto the detector as noted by the clusters of single ion events, and in some cases, these clusters can reveal charge states. For particles of the same charge, it is expected that ions will impart the same energy on impact with the detector surface; however, interestingly, a slight increase in energy was observed with increasing multimeric cluster size. At present, the origin of this observation is not well understood but is believed to be due to a combination of higher ion internal energy and other collision processes.

When looking at signals lower in energy than the singly charged ions (see dashed rectangle in Figure 1b), a few low abundant features are resolved. At identical m/z values of the $[M + X]^+$, $[2M + 2X]^+$, and $[3M + 3X]^+$ ions, low-energy signals are observed to decrease slightly with increasing m/z. These low-energy signals are believed to result from metastable fragmentation. In metastable ion fragmentation inside a TOF mass analyzer, the ion undergoes dissociation in the flight tube after exiting the ion source. The ion is fully accelerated; thus, fragment ions will carry the same velocity as the metastable precursor ion and strike the detector at the same time, providing an identical m/z.[62] However, these fragment ions will be detected at energies less than that of the precursor ion where the energy partitioning among fragments follows the mass partitioning from precursor ions to fragments. As shown in Figure 1, some fractions of $[M + X]^+$, $[2M + X]^+$, and $[3M + X]^+$ precursor ions are observed to undergo metastable fragmentation and lose a small amount of mass prior to impacting the detector. At present, the energy resolution of the STJ detectors is not sufficient and/or the energy spread of these low-energy fragments is too large for the determination of exact compositions, but the fragment mass is clearly a small fraction of the intact NP. We propose that some surface-"labile" material of the NPs, for example, the organic ligand coat, fragments from the core in a metastable fragmentation scheme similar to what has been observed for zinc oxide NPs.[57] The low-energy events observed with the PbS QDs could represent loss of the TOPO coat. There is also a trend in the metastable fragmentation pattern, in which precursor ions of larger m/z (multimers) lose a greater fraction of mass. This may reflect time constraints associated with the dissociation process. Specifically, ions of higher mass (and larger m/z when z is the same) will have lower ion velocities, allowing for longer flight times prior to detection. These longer flight times may provide the additional time needed to localize the energy required to break bonds prior to detection.

One additional feature observed in the LDI mass spectrum of PbS QDs was the high-energy data points which represent primarily doubly charged ion impacts but can also include simultaneous detector hits of two singly charged ions each at 20 keV onto a single STJ element within the detector pulse decay time (~3 μs). These peaks are most likely due to multiply charged multimers because such ions would account for peaks

DOI: 10.1021/acsnano.7b08541
ACS Nano 2018, 12, 2591−2602

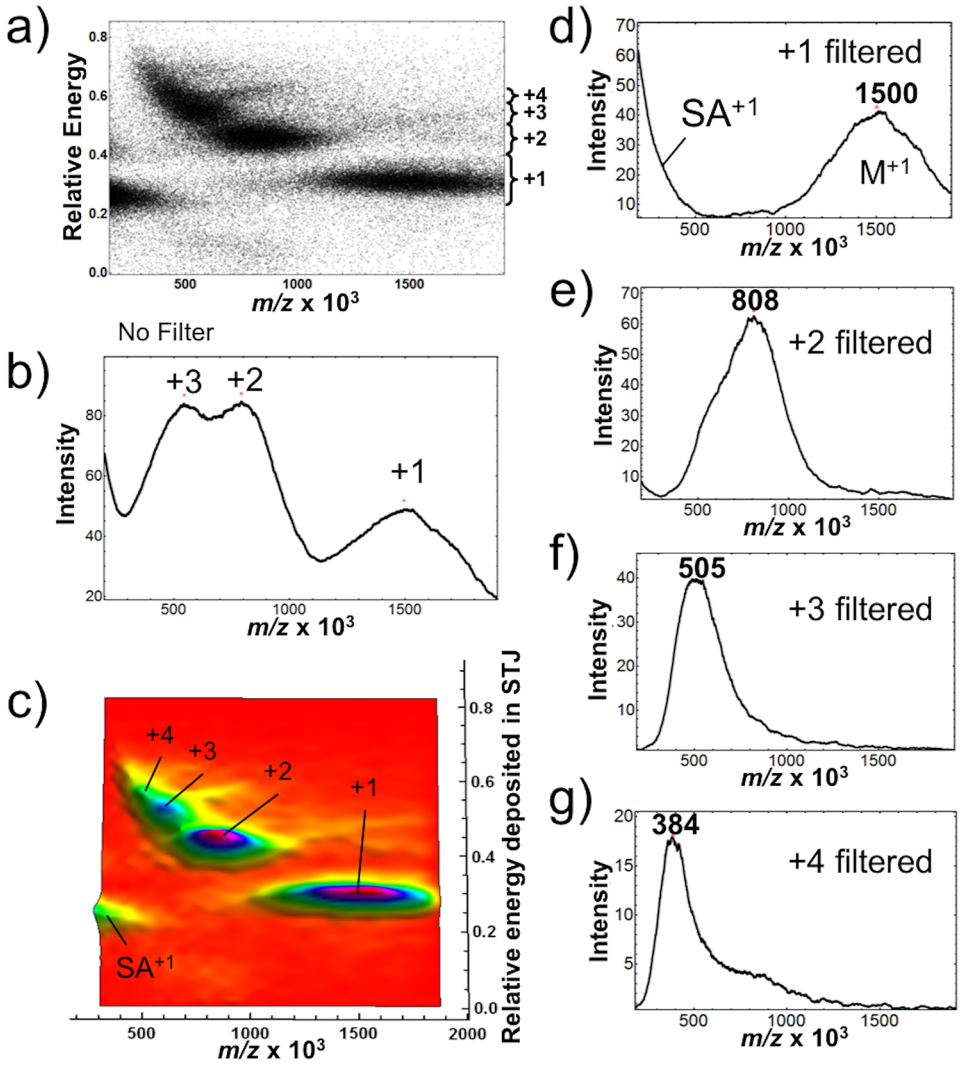

Figure 4. MALDI-TOF-STJ MS analysis of PEGylated core−shell QDs which emit at a wavelength of 800 nm. The $[M + X]^+$ ion increases in mass after PEGylation. (a) Energy scatterplot mass spectrum with clusters at different charge states. (b) 2D mass spectrum of all points from the data in (a). Note the overlap among charge states as a result of nonuniform dispersity among QDs. (c) Top view of the 3D mass spectrum of the data showing peak maximum, which allows ready identification of the different charge states present. (d−g) 2D mass spectra of separated charge states (+1 to +4), labeled with peak m/z values of the distributions. Isolation of the singly charged +1 ions *via* energy filtering refines the mass of the PEGylated QDs to 1500 kDa. Each PEG chain has a mass of ∼2 kDa. The water-soluble carboxyl-functionalized amphiphilic polymer-coated QDs shown in Figure 3 increased in mass from 734 to 1500 kDa, an increase of 761 kDa. This corresponds to an average labeling of these carboxyl-functionalized amphiphilic polymer-coated QDs with ∼383 PEG chains/QD.

at m/z 3/2 and 5/2 for the singly charged particle at m/z ∼2.94 × 10^5 and 4.90 × 10^5, respectively. As a result, a charge state of +2 is assigned to this region of higher-energy points, as shown in Figure 1b. Also noted in this higher-energy region of the spectrum is a weak signal due to metastable fragmentation of the multimeric ions, $[nM + 2X]^{+2}$, again, with slightly lower energies deposited as a result of the lower energies of ion impact.

In addition to the PbS QDs, larger QDs were analyzed using STJ cryodetection MS. Figure 2 shows results from the LDI-TOF-STJ MS analysis of near-infrared (NIR) emitting (800 nm) core−shell QDs. These NPs are composed of a cadmium selenide (CdSe) core layered with cadmium telluride (CdTe), CdSe, and zinc sulfide (ZnS) layers outward followed by TOPO on the surface, causing them to be soluble only in organic solvents (organosols). Figure 2a shows the energy scatterplot mass spectrum generated from the 800 nm emitting core−shell QDs. At the singly charged energy level, two distinct ion clusters are observed as noted by the two dashed rectangles in Figure 2a. The energy-filtered mass spectrum, using the data inside these rectangles, is shown in Figure 2b. These singly charged features have been assigned to monomeric, $[M + X]^+$, and dimeric, $[2M + X]^+$, ion distributions at m/z 4.02 × 10^5 and 9.60 × 10^5, respectively. The strong dimeric ion observed at ∼90% relative abundance is an interesting feature for such large particles that have increased internal energy due to LDI. However, the dimeric peak at m/z 9.60 × 10^5 is significantly higher than predicted by twice the m/z of the 4.02 × 10^5 monomeric peak. This higher dimer mass may represent less fragmentation than observed from the monomer or some yet unknown chemistry that may play a role in the formation of the dimer. There also appears to be an unresolved distribution shown as a shoulder centered at m/z ∼ 8.00 × 10^5 (see Figure 2b,c), which would agree better with the mass calculated from the monomer. These QDs also show lower-energy distributions with significant relative abundances of >50%, which are

DOI: 10.1021/acsnano.7b08541
ACS Nano 2018, 12, 2591−2602

assigned to metastable fragments originating from the singly charged precursor ions. The 3D mass spectrum in Figures 2c highlights the abundance of the precursor ion relative to these metastable fragment ions. The higher abundance of metastable fragments suggests that these QDs are less stable under LDI conditions than the PbS QDs. Also observed was the doubly charged ion, $[M + 2X]^{2+}$, at 30% relative abundance at m/z 2.13 × 10^5 (see solid blue oval in Figure 2a).

Water-soluble 800 nm emitting core−shell QDs with surface-protecting carboxyl-functionalized amphiphilic polymer ligands were analyzed next by MALDI-TOF-STJ MS. The softer technique of MALDI utilizing sinapinic acid (SA) as the matrix was used to reduce fragmentation of these NPs. These water-soluble QDs were observed to give a signal-to-noise ratio by MALDI higher than that observed for the organosol QDs obtained using LDI (compare Figure 2 to Figure 3). The MALDI signal improvement is a reflection of the ability of the matrix to surround the water-soluble particles and to lift the particles while protecting them from the laser energy. As shown in the mass spectra in Figure 3a,b,d, four distinct peaks were observed that corresponded to $[M + X]^+$ and $[M + 2X]^{2+}$ at m/z 7.34 × 10^5 and 3.73 × 10^5, and metastable fragment ion peaks originating from both the singly and doubly charged precursor ions were observed below these peaks at m/z 7.76 × 10^5 and 3.91 × 10^5. These results are similar to the LDI data of the organosol core−shell QDs shown in Figure 2 in that both the +1 and +2 charge states are observed, and they undergo metastable fragmentation. However, compared to the organosol QDs analyzed by LDI in Figure 2, the relative abundance of metastable fragmentation from the singly charged particle is markedly reduced, as one would expect when using MALDI. The spectrum also lacks the signature mass peak of a dimeric species. By selectively filtering signals based on ion energies detected at the STJs, a 2D mass spectrum was plotted in Figure 3c for the three most abundant ion populations observed. Using this energy-filtering tool and the 3D mass spectrum for enhanced visualization in Figure 3d, it was determined that the metastable fragments from the $[M + X]^+$ ions were at ∼25% relative abundance.

Because the cores of both organosol and water-soluble QDs emitting at 800 nm were expected to be of a similar size, and if we assume that the total coat mass of the two different ligands is similar, the mass difference between these particles should be relatively small. However, a ∼339 kDa mass difference was measured between the organosol (Figure 2) and water-soluble (Figure 3) QDs. This mass difference was much larger than what could be attributed to the ligand loading. We propose that at least some of the mass difference is due to in-source fragmentation of the ligand coat by LDI. This has indeed been noted by others studying nanocrystalline gold particles.[63−66] For QDs using LDI, the high flux of photons is absorbed directly by the NPs rather than by the matrix, such as SA, in MALDI. As a result, the large difference between molecular weight determinations in Figure 2 *versus* that in Figure 3 suggests that the 339 kDa mass loss likely included both the surface ligands of the QDs and some additional mass from the core.

NPs have been utilized *in vivo* with applications ranging from tissue imaging to targeted drug delivery.[23,67−69] In addition to concerns about cytotoxicity, researchers are often faced with the challenge of synthesizing NPs that are water-soluble and remain stable in physiological conditions.[69−71] A technique often employed to enhance water solubility and biocompatibility of NPs is to coat their surfaces with polar polymers.[72,73] For example, polyethylene glycol (PEG) coupled to NPs can increase solubility and protect the particles from the immune system of the host.[74] These polymers can also be functionalized to bind small molecules and biomacromolecules for targeted delivery to sites within the host.[22,24,25,69] Mass spectra of water-soluble carboxyl QDs that have been surface PEGylated are shown in Figure 4.

The energy scatterplot mass spectrum generated by the MALDI-TOF-STJ MS analysis of PEGylated 800 nm emitting core−shell QDs is shown in Figure 4a. This QD forms ions readily by MALDI as noted in the unfiltered spectrum in Figure 4, which consists of ∼95000 ion impacts. Both singly and multiply charged ions of the intact PEGylated QDs were observed. Figure 4b shows a traditional 2D mass spectrum. Due to the broad mass dispersity of the intact PEGylated QDs, m/z values of multiply charged ions overlap significantly. The ability to separate the data into a third dimension *via* measurement of the relative energy imparted to the STJ detectors allows charge states to be resolved, thus yielding additional information. In addition, accurate energy separation can result in better mass assignments. Figure 4a,c,d shows the $[M + X]^+$ ion as a broad distribution centered at m/z ∼ 1.500 × 10^6. Using energy filtering, individual charge states from +1 to +4 can be isolated as shown in Figure 4d−g. Multiply charged ions, $[M + 2X]^{2+}$, $[M + 3X]^{3+}$, and $[M + 4X]^{4+}$ were detected at m/z 8.08 × 10^5, 5.05 × 10^5, and 3.84 × 10^5, respectively, providing an average mass determination of 1516 kDa with a σ of 1.1%.

The observation of the singly charged PEGylated QDs at m/z ∼ 1.500 × 10^6 (MW_{avg} ∼1.5 MDa) demonstrates the high detection efficiency of STJ for these macromolecules at low charge states. The ability to detect ions at low charge states is especially advantageous for NPs as synthetic methodologies generate large variations in particle size, which are readily observed as peak broadening in the m/z dimension. Using the most abundant mass of the broad +1 charge state, the molecular weight of the PEGylated QD (Figure 4) was compared to the intact carboxyl-functionalized amphiphilic polymer-coated QDs (Figure 3). Assuming that the core structure of the QDs was the same, the significant difference in mass between these particles is proposed to account for the amount of ligand loading of the surface coatings. At an average molecular weight of 2 kDa for the PEG ligands, the ∼766 kDa mass difference between carboxyl-functionalized amphiphilic polymer-coated (Figure 3) and PEGylated (Figure 4) QDs provides a ligand loading number of ∼383 PEG chains on the surface of the QD.

We next analyzed core−shell QDs which emit at 655 nm by LDI-TOF-STJ MS and MALDI-TOF-STJ MS. These QDs were analyzed biomolecule-free and also conjugated to either cholera toxin B (CTB), MW ∼ 11.6 kDa, or human serum transferrin (HuTf), MW ∼ 75.2 kDa. Cholera toxin B (CTB)-conjugated QDs have been used as an alternative to polyarginine labeling to minimize particle aggregation upon internalization in cellular labeling studies.[75] Transferrin-conjugated QDs undergo receptor-mediated endocytosis when bound to transferrin receptors to bring QDs into cells.[68] Both CTB- and HuTf-labeled QDs were biologically active.[76] The biomolecule-free organosol core−shell QDs were composed of a CdSe core surrounded by a ZnS layer prior to surface protection in contrast to the four-layer composition of the 800 nm emitting core−shell QDs shown in Figures 2−4. The LDI-TOF-STJ MS analysis of organosol QDs prior to

DOI: 10.1021/acsnano.7b08541
ACS Nano 2018, 12, 2591−2602

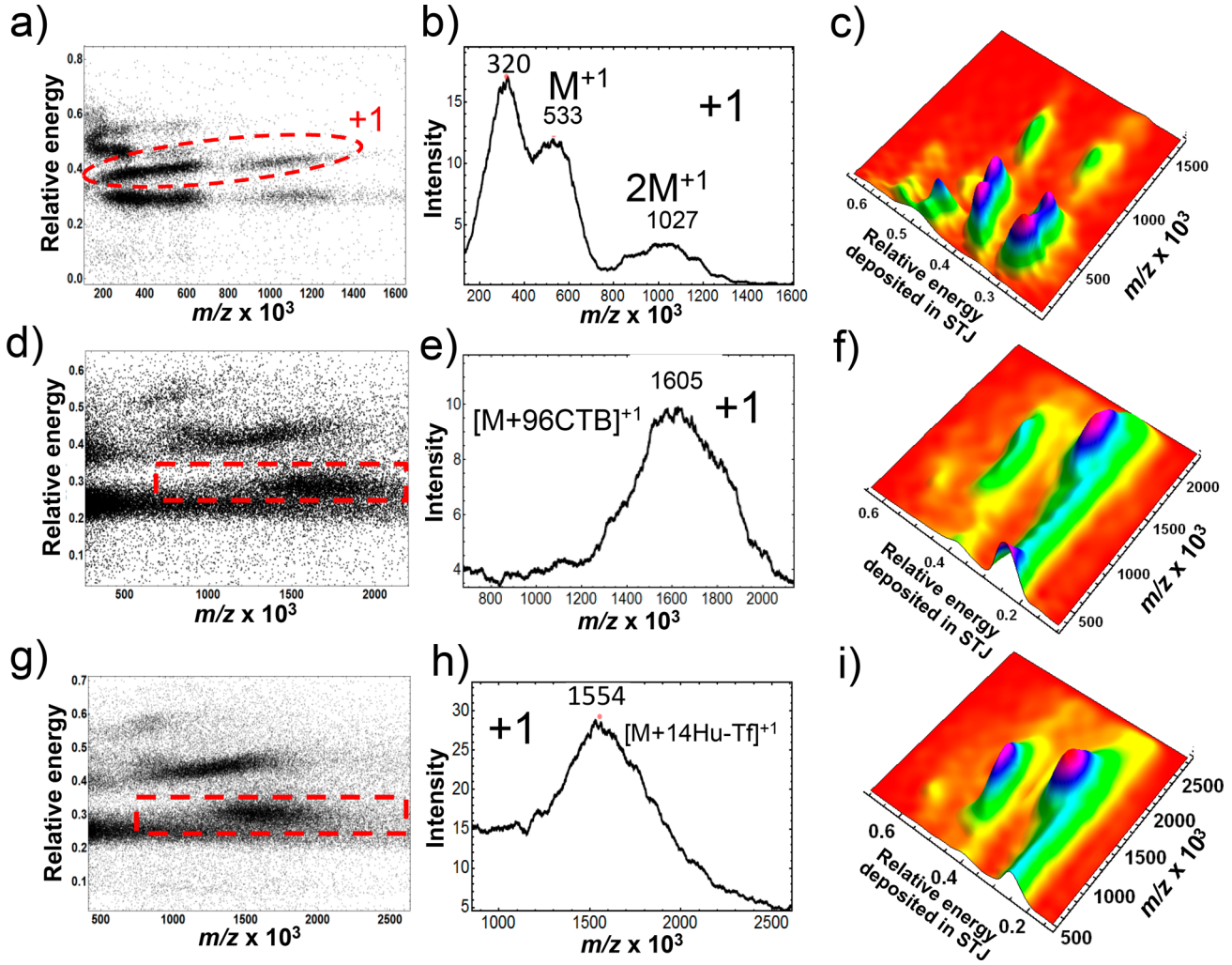

Figure 5. LDI-TOF-STJ MS mass spectrum of organosol core−shell QDs emitting at 655 nm without biomolecule conjugation and MALDI-TOF-STJ MS with biomolecule ligands. (a) Energy scatterplot of the biomolecule free QDs. As in Figures 2 and 3, metastable fragmentation was also observed. (b) 2D mass spectrum of singly charged ions from (a) with the suspected intact QDs appearing at m/z 5.33 × 10^5. Singly charged dimers were also observed at m/z 1.027 × 10^6. The peak at m/z 3.20 × 10^5 is tentatively assigned to be LDI fragments generated through in-source fragmentation prior to ion acceleration. (c) 3D mass spectrum of all the points in (a). (d−f) MALDI mass spectra of carboxyl-functionalized amphiphilic polymer-coated core−shell QDs that were covalently coupled with cholera toxin B (CTB) (MW ∼ 11.6 kDa). (g−i) MALDI mass spectra of carboxyl-functionalized amphiphilic polymer-coated core−shell QDs that were covalently coupled with human serum transferrin (HuTf) (MW ∼ 75.2 kDa). The average number of protein molecules attached was calculated to be 96 and 14 for CTB-QDs and HuTf-QDs, respectively. Water-soluble, 655 nm emitting carboxyl-functionalized amphiphilic polymer-coated core−shell QDs were unavailable.

bioconjugation is shown in Figure 5a−c. This bioligand-free particle served as a reference when compared to the bioconjugated QDs. The energy scatterplot in Figure 5a shows multiple features resolved in both m/z and particle energy. Figure 5b shows the energy-filtered 2D mass spectrum for singly charged ions. Three distinct peaks are observed. The peak at m/z 5.33 × 10^5 has been assigned to $[M + X]^+$, and the peak at m/z 1.027 × 10^6 has been assigned to a dimer, $[2M + X]^+$. The singly charged partially resolved peak at m/z 3.20 × 10^5 is believed to be fragments of the intact QDs after partial fragmentation in the ion source prior to acceleration; however, heterogeneity of NP production could also account for this lower m/z distribution. LDI is known to be a more energetic process, and these data suggest that LDI is not the ionization method of choice as it can lead to increased fragmentation of these particles. Figure 5c shows the 3D mass spectrum from the LDI-TOF-STJ MS analysis of the organosol core−shell QDs. The 3D mass spectrum more clearly shows the peak maxima of the multiply charged and metastable fragment ions through the added energy dimension.

The MALDI-TOF-STJ MS analysis of QDs conjugated to CTB is shown in Figure 5d−f, whereas QDs conjugated to HuTf are shown in Figure 5g−i. The energy scatterplot for CTB-conjugated QDs is shown in Figure 5d, and the singly charged energy-filtered 2D mass spectrum and full 3D mass spectrum are shown in Figure 5e,f, respectively. Intact CTB-conjugated QDs were detected singly charged at m/z 1.605 × 10^6 (MW_{ave} of ∼1.61 MDa). Using the difference between the $[M + X]^+$ peaks in Figure 5b,e (m/z 1.117 × 10^6), it was estimated that ∼96 CTB molecules (∼11.6 kDa) were conjugated to the QD. In a similar approach, HuTf-conjugated QDs were analyzed, and these results are shown in Figure 5g−i. The energy scatterplot for HuTf-conjugated QDs is shown in Figure 5g, whereas the singly charged energy-filtered 2D mass

DOI: 10.1021/acsnano.7b08541
ACS Nano 2018, 12, 2591−2602

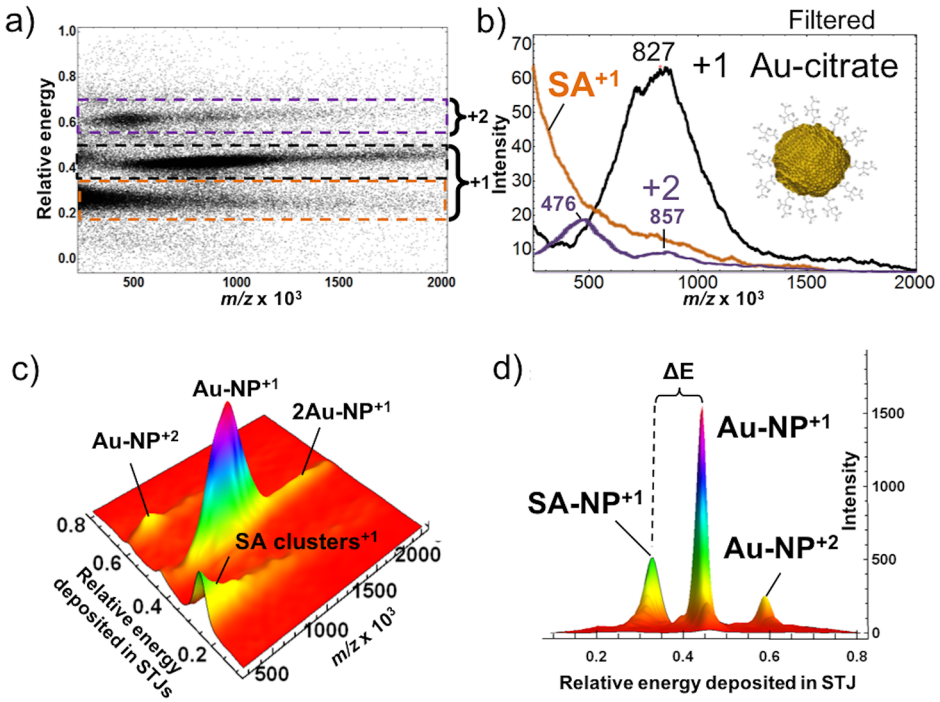

Figure 6. MALDI-TOF-STJ MS of Au NPs. (a) Energy scatterplot mass spectrum of Au NPs, showing singly and doubly charged ions. While a lower-energy signal band (orange box) was also observed for Au NPs, this feature has been assigned to clusters of organic matrix ions from sinapinic acid used in the MALDI process. (b) 2D mass spectrum of energy-filtered +1 and +2 charge states. The inset shows a space-filling model for the Au NPs coated with citrate. The black trace represents singly charged Au NP ions that have an apex at m/z 8.27 × 10^5, which represents ~4544 Au atoms free from citrate. The mass of the Au NP (~827 kDa) is significantly higher than the calculated mass for a 5 nm Au particle (761 kDa). The manufacturer only provided the Au NPs diameter to one significant figure. The purple trace represents doubly charged Au NP ions at m/z 4.76 × 10^5, as well as doubly charged dimers at m/z 8.57 × 10^5. The orange trace represents clusters of SA matrix ions. The neutral mass calculated from the doubly charged Au NP was found to be 952 kDa and may reflect the increased probability of larger Au NPs obtaining a second charge. (c) 3D mass spectrum showing the base peak to be +1 and the +2 at ~30% relative abundance. (d) Relative energy deposited into the STJ detectors for SA matrix ion clusters, singly charged Au NPs, and doubly charged Au NPs. The Au NPs show a significantly higher energy (ΔE) deposited into the STJ detector as compared to SA clusters of the same mass.

spectrum and full 3D mass spectrum are shown in Figure 5h,i, respectively. HuTf-conjugated QDs were detected intact and singly charged at m/z 1.554 × 10^6 (MW_{ave} of ~1.55 MDa). The mass difference between the $[M + X]^+$ peaks of the organosol core−shell QD reference (Figure 5b) and that of the HuTf-conjugated QD (Figure 5h) of m/z 1.021 × 10^6 suggested that ~14 HuTf molecules (~75.2 kDa) were conjugated on the surface of the QD. The ligand loading calculation was based on LDI data in Figure 5c and not MALDI data for organosol QDs. As the former ionization method uses direct ablation of material with laser irradiation, there is no possibility for matrix molecules to contribute to the mass of these QDs *via* adduction (as it is common for larger species). A possible downside to LDI is increased fragmentation, as discussed above, which can also alter the results. In any regard, these results demonstrate that a specialized ultrahigh mass MS technique, such as MALDI MS with STJ cryodetection, allows efficient detection of macromolecules above 1 MDa and allows estimation of cargo loading of specific biomolecules on the surface of NPs.

As a final example of the utility of STJ cryodetection MS for studying NPs, a metallic NP whose core consisted of gold (Au) atoms was analyzed. MALDI-TOF-STJ MS results from the analysis of 5 nm Au NPs protected by citrate ligands are shown in Figure 6.

The energy scatterplot in Figure 6a shows three distinct clusters of points. Upon energy filtering for the +1 charge state, the 2D mass spectrum in Figure 6b displays the singly charged $[M + X]^+$ distribution, which has a maxima at m/z 8.27 × 10^5, whereas filtering for the +2 charge state shows the doubly charged ion distribution, $[M + 2X]^{2+}$ at a maxima of m/z 4.76 × 10^5. Due to Au NP peak dispersity and the current limitations in mass resolution, it was not clear whether citrate was retained on the surface after the MALDI processes, but if so, the mass contribution was expected to be small relative to the mass of the Au core. Based on the measurement of mass of the singly charged ions, the expected m/z value for the doubly charged ions was expected to be centered at m/z 4.14 × 10^5. The difference between the measured m/z value for the doubly charged ion (m/z 4.76 × 10^5) and that of the predicted value (m/z 4.14 × 10^5) may be due to lower ion abundance statistics for the doubly charged ion, which was present at ~30% abundance relative to the singly charged ion. Alternatively, larger Au NPs may preferentially favor two charges, thus shifting the average m/z for the +2 charge state higher.

Using the bulk density of gold (19.32 g cm^{-1}) and assuming that citrate was fully stripped from the Au core, it was determined that the mean diameter of the detected Au NPs was 5.14 nm. This is in good agreement with the nominal 5 nm value supplied by the manufacturer. A 5.00 nm Au NP was estimated to have a mass of ~761 kDa. As shown by the Au core size estimates from the MALDI-TOF-STJ MS results and 5 nm nominal core size calculations, a small change in particle diameter can account for a significant change in the mass of the particle. This STJ MS methodology may provide a more

DOI: 10.1021/acsnano.7b08541
ACS Nano 2018, 12, 2591−2602

accurate size and dispersity measurement as it is based solely on molecular mass determinations. Approximately 74000 Au NP ion impacts were acquired to generate this mass spectrum.

As discussed previously, signals observed below the energy of the singly charged ions are typically assigned to metastable fragments if they are aligned in m/z but with lower energy. A distribution was shown in Figure 6 for the Au NP MALDI-TOF-STJ MS data which tailed from m/z 5.00×10^5 to 1.000×10^6 between the relative energy deposited values of 0.2 to 0.3. In this case, the ion signal was assigned to clusters of SA matrix. The exponential decay in abundance of the lower-energy SA signal is commonly observed for small-molecule matrix clusters in MALDI MS, and as shown here, these signals can be observed above m/z 5.00×10^5. The significant difference in energy (ΔE) between singly charged 5 nm Au NPs and SA organic matrix cluster ions is shown in Figure 6c,d. We have found that signals detected at the lower-energy levels are associated with singly charged organic ions (*i.e.*, biomolecules, synthetic polymers, *etc.*). Metallic or inorganic NPs, as shown here, yielded a higher-energy response by STJ MS than organic ions given the same kinetic energy and mass. Interestingly, the Au NPs yielded the highest STJ energy response of all particles analyzed, followed by the less dense PbS QDs and core−shell Cd-based QDs. We hypothesize that there is a correlation between physiochemical properties of these NPs such as the internal energy or heat capacity of these ions and the degree to which various collisional processes occur compared to the measured STJ response.

CONCLUSIONS

In this report, we demonstrated that MALDI and LDI STJ cryodetection MS allows characterization of nanomaterials at ultrahigh mass. Using this approach, average molecular weights and dispersities can be readily determined for low charge state heavy ions at m/z well above 1.00×10^5. While the mass spectrometer used has a relatively low resolving power, all NP mass peaks in this report were broad primarily due to the large dispersity of sizes as a result of the synthetic processes. PbS QDs were found to readily form multimers by LDI-TOF-STJ MS when compared to the other NPs analyzed. Many QDs undergo metastable fragmentation by LDI and MALDI, evidenced by signals detected at energy levels less than that of a singly charged ion but with m/z alignment. In some instances, and especially by LDI, in-source fragmentation was observed, whereby the m/z of detected ions was reduced due to fragmentation prior to ion acceleration. The energy measurements enabled by the use of STJ cryodetection allow for contributions from m/z-aligned fragments to be discriminated from the total ion current, which is currently not possible with conventional ionizing detectors. Future energy resolution improvements of STJ cryodetectors should allow for an improved determination of relative NP stability using information gained from metastable fragmentation patterns.

Combining LDI and MALDI approaches allows characterization of intact NPs but also provides a means to investigate NP composition, where fragmentation is expected to reflect aspects of particle stability and surface structure. For example, when attempting to measure the intact mass, dispersity, and particle stability of the NPs, MALDI was employed, whereas LDI was used to study more robust NPs or to further investigate particle stability under more rigorous conditions. With further development, STJ cryodetection may be able to provide additional NP characterization information beyond molecular weight, dispersity, and stability by invoking characteristic responses of the STJ detectors in a single MS experiment. Chemical information, such as the extent of ligand loading, is also readily available by MALDI STJ MS through measurement of the reactant and product masses, similar to what is typically afforded by TGA.

After analyzing these NPs, we observed intriguing differences between the detected energy responses for various NP compositions. The reasons for these differences are not well understood, but clearly many physical and chemical processes, such as energy transfer, would occur during the collision of an ion with a surface. As the detector response is proportional to energy deposited by the impinging particle, redistributions of energy between internal degrees of freedom and the energy transferred to the detector would affect the readout. These different detector responses may provide useful analytical information related to the physiochemical properties of each type of NP and the collision processes with which they undergo.

METHODS

Chemicals. Water, acetonitrile, and acetone as solvents were of HPLC grade and purchased from Fisher Scientific (Fair Lawn, NJ). Sinapinic acid matrix was obtained from Sigma-Aldrich (St. Louis, MO). PbS QDs with 1311 nm emission were a gift from Evident Technologies (Troy, NY) and used as received as a toluene suspension at 2.5 mg/mL. The average size of the PbS cores, as determined by TEM, was ~4.2 nm.[61] CdSe and CdSe + CdTe visible-light-emitting QDs were from Molecular Probes-Invitrogen (Eugene, OR). Organosol CdSe-based core−shell QDs with 800 nm emission were used as received as a decane suspension at 0.9 μM. Water-soluble CdSe-based core−shell QDs with 800 nm emission, coated with carboxyl-functionalized amphiphilic polymers, were used as received as aqueous colloids at 8.0 μM. PEGylated CdSe-based core−shell QDs with 800 nm emission were used as received as aqueous colloids at 2.0 μM. Organosol CdSe-based core−shell QDs with 655 nm emission were used as received as a decane suspension at 1.0 μM. CTB-conjugated and HuTf-conjugated CdSe-based core−shell QDs with 655 nm emission were received as gifts and used as received. Citrate-protected Au NPs (5 nm nominal diameter) were obtained from Sigma-Aldrich (St. Louis, MO) and used as received.

Sample Preparation. For LDI-based experiments (organosol QDs), samples were spotted directly onto the MALDI plate and allowed to air-dry prior to introduction into the mass spectrometer. For MALDI-based experiments with water-soluble NPs, 1−2 μL of SA matrix solution (a saturated solution in 1:1 acetone/water + 0.1% v/v trifluoroacetic acid) was spotted onto the plate, and then 1−2 μL of NPs was added, mixed with a micropipetter directly on the plate, and allowed to dry before introduction into the mass spectrometer.

STJ Cryodetection Mass Spectrometry. LDI/MALDI-TOF analyses were performed on a Macromizer (Comet AG, Flamatt, Switzerland) mass spectrometer equipped with a 16 channel, 200 μm × 200 μm per pixel, STJ cryodetector held at 0.34 K.[54] The sample spot was visually selected, and the optimal area of the spot was empirically established in a series of method development and optimization experiments. Samples were irradiated with a 337 nm nitrogen laser pulsed at 10 Hz with a maximum pulse energy of 260 μJ. The sample plate was held at 20 kV, and the instrument was operated in delayed extraction mode with the grid element pulsed to 17 kV using a delay time of 10 μs. The Einzel lens was fixed at 10 kV for all experiments. Individual STJ detectors were biased at 350 μV with the Helmholtz coil set to 1 A.

Mass calibration at ultrahigh m/z values (>100000) is a relatively new problem that has arisen with the development of heavy ion mass spectrometry. The TOF response of the instrument was calibrated between m/z 3.81×10^5 and 1.617×10^6 using multiply charged ions of the matured capsid (Head II) of bacteriophage HK97 (MW_{avg} =

DOI: 10.1021/acsnano.7b08541
ACS Nano 2018, 12, 2591−2602

12,918,636.96 Da).[58] HK97 Head II was selected as a calibrant due to its monodispersity, ability to multiply charge by MALDI, and because of its stability through natural subunit cross-linking.

An absolute STJ energy calibration was not performed for these data because it was not necessary to determine the spectral assignments. In addition, we discovered that different NPs give significantly different energy responses even at the same m/z and charge state. We determined what energy bands are due to a specific charge state by analyzing the whole spectrum. In general, the +1 charge state was found to fall between 0.3 and 0.5 relative energy deposited into the STJ detectors for these NPs. Although there is some energy overlap, above that energy was assigned to doubly charged or higher charge state ions and below that energy was assigned to metastable fragments.

The acquired data were processed offline in a custom Mathematica program developed in house. An energy correction algorithm was applied to the data using the Mathematica program to minimize variations in energy responses between individual detectors.

AUTHOR INFORMATION

Corresponding Author

*E-mail: mbier@cmu.edu.

ORCID

Logan D. Plath: 0000-0002-3355-7169

Mark E. Bier: 0000-0002-5220-9338

Present Addresses

†(A.A.A.) University of California, San Diego, School of Pharmacy and Pharmaceutical Science, 9500 Gilman Drive #0719, La Jolla, CA 92093.

‡(J.S.F.) Zwanger-Pesiri Radiology, 110 Bi County Boulevard, Farmingdale, NY 11735.

Notes

The authors declare no competing financial interest.

ACKNOWLEDGMENTS

We thank the NSF for funding under Grants DBI 0454980 and CHE 1611146. We thank Fan Wang for help in Mathematica programming. We thank Kayla Leach (Evident Technologies) for the gift of the PbS QDs and for discussion of technical information. We also acknowledge gifts of CdSe and CdTe QDs from Sue Andreko and Byron Ballou of the Molecular Biosensor and Imaging Center (MBIC) at Carnegie Mellon University. Finally, we acknowledge the use of the Center for Molecular Analysis at Carnegie Mellon University.

REFERENCES

(1) Eustis, S.; El-Sayed, M. A. Why Gold Nanoparticles Are More Precious than Pretty Gold: Noble Metal Surface Plasmon Resonance and Its Enhancement of the Radiative and Nonradiative Properties of Nanocrystals of Different Shapes. *Chem. Soc. Rev.* **2006**, *35*, 209−217.

(2) Jelinek, R. *Nanoparticles*; De Gruyter: Berlin, 2015.

(3) Zheng, J.; Zhou, C.; Yu, M.; Liu, J. Different Sized Luminescent Gold Nanoparticles. *Nanoscale* **2012**, *4*, 4073−4083.

(4) Bera, D.; Qian, L.; Tseng, T.; Holloway, P. H. Quantum Dots and Their Multimodal Applications: A Review. *Materials* **2010**, *3*, 2260−2345.

(5) Jain, P. K.; Huang, X.; El-Sayed, I. H.; El-Sayed, M. A. Review of Some Interesting Surface Plasmon Resonance-Enhanced Properties of Noble Metal Nanoparticles and Their Applications to Biosystems. *Plasmonics* **2007**, *2*, 107−118.

(6) Pei, Y.; Zeng, X. C. Investigating the Structural Evolution of Thiolate Protected Gold Clusters from First-Principles. *Nanoscale* **2012**, *4*, 4054−4072.

(7) Shenhar, R.; Rotello, V. M. Nanoparticles: Scaffolds and Building Blocks. *Acc. Chem. Res.* **2003**, *36*, 549−561.

(8) Zhang, J.; Lima, F. H. B.; Shao, M. H.; Sasaki, K.; Wang, J. X.; Hanson, J.; Adzic, R. R. Platinum Monolayer on Nonnoble Metal - Noble Metal Core - Shell Nanoparticle Electrocatalysts for O_2 Reduction. *J. Phys. Chem. B* **2005**, *109*, 22701−22704.

(9) Moisala, A.; Nasibulin, A. G.; Kauppinen, E. I. The Role of Metal Nanoparticles in the Catalytic Production of Single-Walled Carbon Nanotubes — a Review. *J. Phys.: Condens. Matter* **2003**, *15*, S3011−S3035.

(10) Rosi, N. L.; Mirkin, C. A. Nanostructures in Biodiagnostics. *Chem. Rev.* **2005**, *105*, 1547−1562.

(11) Pradeep, T.; Anshup. Noble Metal Nanoparticles for Water Purification: A Critical Review. *Thin Solid Films* **2009**, *517*, 6441−6478.

(12) De, M.; Ghosh, P. S.; Rotello, V. M. Applications of Nanoparticles in Biology. *Adv. Mater.* **2008**, *20*, 4225−4241.

(13) Sonnichsen, C.; Franzl, T.; Wilk, T.; von Plessen, G.; Feldmann, J. Plasmon Resonances in Large Noble-Metal Clusters. *New J. Phys.* **2002**, *4*, 93.1−93.8.

(14) Alivisatos, A. P. Semiconductor Clusters, Nanocrystals, and Quantum Dots. *Science* **1996**, *271*, 933−937.

(15) El-Sayed, M. A. Small Is Different: Shape-, Size-, and Composition-Dependent Properties of Some Colloidal Semiconductor Nanocrystals. *Acc. Chem. Res.* **2004**, *37* (5), 326−333.

(16) Anikeeva, P. O.; Halpert, J. E.; Bawendi, M. G.; Bulovic, V. Quantum Dot Light-Emitting Devices with Electroluminescence Tunable over the Entire Visible Spectrum. *Nano Lett.* **2009**, *9*, 2532−2536.

(17) Han, M.; Gao, X.; Su, J. Z.; Nie, S. Quantum-Dot-Tagged Microbeads for Multiplexed Optical Coding of Biomolecules. *Nat. Biotechnol.* **2001**, *19*, 631−635.

(18) Nozik, A. J. Nanoscience and Nanostructures for Photovoltaics and Solar Fuels. *Nano Lett.* **2010**, *10*, 2735−2741.

(19) Gur, I.; Fromer, N. A.; Geier, M. L.; Alivisatos, A. P. Air-Stable All-Inorganic Nanocrystal Solar Cells Processed from Solution. *Science* **2005**, *310*, 462−465.

(20) Lee, J.; Sundar, V. C.; Heine, J. R.; Bawendi, M. G.; Jensen, K. F. Full Color Emission from II-VI Semiconductor Quantum Dot-Polymer Composites. *Adv. Mater.* **2000**, *12*, 1102−1105.

(21) Huynh, W. U.; Peng, X.; Alivisatos, A. P. CdSe Nanocrystal Rods/Poly(3-Hexylthiophene) Composite Photovoltaic Devices. *Adv. Mater.* **1999**, *11*, 923−927.

(22) Michalet, X.; Pinaud, F. F.; Bentolila, L. A.; Tsay, J. M.; Doose, S.; Li, J. J.; Sundaresan, G.; Wu, A. M.; Gambhir, S. S.; Weiss, S. Quantum Dots for Live Cells, *In Vivo* Imaging, and Diagnostics. *Science* **2005**, *307*, 538−544.

(23) Chan, W. C. W.; Maxwell, D. J.; Gao, X.; Bailey, R. E.; Han, M.; Nie, S. Luminescent Quantum Dots for Multiplexed Biological Detection and Imaging. *Curr. Opin. Biotechnol.* **2002**, *13*, 40−46.

(24) Prapainop, K.; Witter, D. P.; Wentworth, P. A Chemical Approach for Cell-Specific Targeting of Nanomaterials: Small-Molecule-Initiated Misfolding of Nanoparticle Corona Proteins. *J. Am. Chem. Soc.* **2012**, *134*, 4100−4103.

(25) Gao, X.; Cui, Y.; Levenson, R. M.; Chung, L. W. K.; Nie, S. *In Vivo* Cancer Targeting and Imaging with Semiconductor Quantum Dots. *Nat. Biotechnol.* **2004**, *22*, 969−976.

(26) Amirav, L.; Alivisatos, A. P. Photocatalytic Hydrogen Production with Tunable Nanorod Heterostructures. *J. Phys. Chem. Lett.* **2010**, *1*, 1051−1054.

(27) Zong, X.; Yan, H.; Wu, G.; Ma, G.; Wen, F.; Wang, L.; Li, C. Enhancement of Photocatalytic H_2 Evolution on CdS by Loading MoS_2 as Cocatalyst under Visible Light Irradiation. *J. Am. Chem. Soc.* **2008**, *130*, 7176−7177.

(28) Zucker, R. M.; Massaro, E. J.; Sanders, K. M.; Degn, L. L.; Boyes, W. K. Detection of TiO_2 Nanoparticles in Cells by Flow Cytometry. *Cytometry, Part A* **2010**, *77A*, 677−685.

(29) Gouadec, G.; Colomban, P. Raman Spectroscopy of Nanomaterials: How Spectra Relate to Disorder, Particle Size and Mechanical Properties. *Prog. Cryst. Growth Charact. Mater.* **2007**, *53*, 1−56.

DOI: 10.1021/acsnano.7b08541
ACS Nano 2018, 12, 2591−2602

(30) Sfeir, M. Y.; Beetz, T.; Wang, F.; Huang, L.; Huang, X. M. H.; Huang, M.; Hone, J.; O'Brien, S.; Misewich, J. A.; Heinz, T. F.; Wu, L.; Zhu, Y.; Brus, L. E. Optical Spectroscopy of Individual Single-Walled Carbon Nanotubes of Defined Chiral Structure. *Science* **2006**, *312*, 554−556.
(31) Hemraj-Benny, T.; Banerjee, S.; Sambasivan, S.; Balasubramanian, M.; Fischer, D. A.; Eres, G.; Puretzky, A. A.; Geohegan, D. B.; Lowndes, D. H.; Han, W.; Misewich, J. A.; Wong, S. S. Near-Edge X-Ray Absorption Fine Structure Spectroscopy as a Tool for Investigating Nanomaterials. *Small* **2006**, *2*, 26−35.
(32) Cuenot, S.; Frétigny, C.; Demoustier-Champagne, S.; Nysten, B. Surface Tension Effect on the Mechanical Properties of Nanomaterials Measured by Atomic Force Microscopy. *Phys. Rev. B: Condens. Matter Mater. Phys.* **2004**, *69*, 165410.
(33) Zeng, C.; Chen, Y.; Kirschbaum, K.; Lambright, K. J.; Jin, R. Emergence of Hierarchical Structural Complexities in Nanoparticles and Their Assembly. *Science* **2016**, *354*, 1580−1584.
(34) Wu, Z.; Jiang, D.; Lanni, E.; Bier, M. E.; Jin, R. Sequential Observation of $Ag_nS_4^-$ $(1 \leq n \leq 7)$ Gas Phase Clusters in MS/MS and Prediction of Their Structures. *J. Phys. Chem. Lett.* **2010**, *1*, 1423−1427.
(35) Negishi, Y.; Takasugi, Y.; Sato, S.; Yao, H.; Kimura, K.; Tsukuda, T. Magic-Numbered Au_n Clusters Protected by Glutathione Monolayers (n = 18, 21, 25, 28, 32, 39): Isolation and Spectroscopic Characterization. *J. Am. Chem. Soc.* **2004**, *126*, 6518−6519.
(36) Dass, A.; Stevenson, A.; Dubay, G. R.; Tracy, J. B.; Murray, R. W. Nanoparticle MALDI-TOF Mass Spectrometry without Fragmentation: $Au_{25}(SCH_2CH_2Ph)_{18}$ and Mixed Monolayer $Au_{25}(SCH_2CH_2Ph)_{18-x}(L)_x$. *J. Am. Chem. Soc.* **2008**, *130*, 5940−5946.
(37) Fields-Zinna, C. A.; Sampson, J. S.; Crowe, M. C.; Tracy, J. B.; Parker, J. F.; DeNey, A. M.; Muddiman, D. C.; Murray, R. W. Tandem Mass Spectrometry of Thiolate-Protected Au Nanoparticles $Na_xAu_{25}(SC_2H_4Ph)_{18-y}(S(C_2H_4O)_5CH_3)_y$. *J. Am. Chem. Soc.* **2009**, *131*, 13844−13851.
(38) Fields-Zinna, C. A.; Sardar, R.; Beasley, C. A.; Murray, R. W. Electrospray Ionization Mass Spectrometry of Intrinsically Cationized Nanoparticles, $[Au_{144/146}(SC_{11}H_{22}N(CH_2CH_3)_3^+)_x(S(CH_2)_5CH_3)_y]^{x+}$. *J. Am. Chem. Soc.* **2009**, *131*, 16266−16271.
(39) Qian, H.; Zhu, M.; Lanni, E.; Zhu, Y.; Bier, M. E.; Jin, R. Conversion of Polydisperse Au Nanoparticles into Monodisperse Au_{25} Nanorods and Nanospheres. *J. Phys. Chem. C* **2009**, *113*, 17599−17603.
(40) Qian, H.; Eckenhoff, W. T.; Bier, M. E.; Pintauer, T.; Jin, R. Crystal Structures of Au_2 Complex and Au_{25} Nanocluster and Mechanistic Insight into the Conversion of Polydisperse Nanoparticles into Monodisperse Au_{25} Nanoclusters. *Inorg. Chem.* **2011**, *50*, 10735−10739.
(41) Wu, Z.; Lanni, E.; Chen, W.; Bier, M. E.; Ly, D.; Jin, R. High Yield, Large Scale Synthesis of Thiolate-Protected Ag_7 Clusters. *J. Am. Chem. Soc.* **2009**, *131*, 16672−16674.
(42) Johnson, B. F. G.; McIndoe, J. S. Spectroscopic and Mass Spectrometric Method for the Characterisation of Metal Clusters. *Coord. Chem. Rev.* **2000**, *200−202*, 901−932.
(43) Geno, P. W.; Macfarlane, R. D. Secondary Electron Emission Induced by Impact of Low-Velocity Molecular Ions on a Microchannel Plate. *Int. J. Mass Spectrom. Ion Processes* **1989**, *92*, 195−210.
(44) Twerenbold, D.; Gerber, D.; Gritti, D.; Gonin, Y.; Netuschill, A.; Rossel, F.; Schenker, D.; Vuilleumier, J. L. Single Molecule Detector for Mass Spectrometry with Mass Independent Detection Efficiency. *Proteomics* **2001**, *1*, 66−69.
(45) Westmacott, G.; Frank, M.; Labov, S.; Benner, W. Using a Superconducting Tunnel Junction Detector to Measure the Secondary Electron Emission Efficiency for a Microchannel Plate Detector Bombarded by Large Molecular Ions. *Rapid Commun. Mass Spectrom.* **2000**, *14*, 1854−1861.
(46) Bich, C.; Scott, M.; Panagiotidis, A.; Wenzel, R. J.; Nazabal, A.; Zenobi, R. Characterization of Antibody-Antigen Interactions: Comparison between Surface Plasmon Resonance Measurements and High-Mass Matrix-Assisted Laser Desorption/Ionization Mass Spectrometry. *Anal. Biochem.* **2008**, *375*, 35−45.
(47) Alvarez, M. M.; Chen, J.; Plascencia-Villa, G.; Black, D. M.; Griffith, W. P.; Garzón, I. L.; José-Yacamán, M.; Demeler, B.; Whetten, R. L. Hidden Components in Aqueous "Gold-144" Fractionated by PAGE: High-Resolution Orbitrap ESI-MS Identifies the Gold-102 and Higher All-Aromatic Au-pMBA Cluster Compounds. *J. Phys. Chem. B* **2016**, *120*, 6430−6438.
(48) van de Waterbeemd, M.; Fort, K. L.; Boll, D.; Reinhardt-Szyba, M.; Routh, A.; Makarov, A.; Heck, A. J. R. High-Fidelity Mass Analysis Unveils Heterogeneity in Intact Ribosomal Particles. Nat. *Nat. Methods* **2017**, *14* (3), 283−286.
(49) Fort, K. L.; van de Waterbeemd, M.; Boll, D.; Reinhardt-Szyba, M.; Belov, M. E.; Sasaki, E.; Zschoche, R.; Hilvert, D.; Makarov, A. A.; Heck, A. J. R. Expanding the Structural Analysis Capabilities on an Orbitrap-Based Mass Spectrometer for Large Macromolecular Complexes. *Analyst* **2018**, *143*, 100−105.
(50) Twerenbold, D.; Vuilleumier, J.; Gerber, D.; Tadsen, A.; van den Brandt, B.; Gillevet, P. M. Detection of Single Macromolecules Using a Cryogenic Particle Detector Coupled to a Biopolymer Mass Spectrometer. *Appl. Phys. Lett.* **1996**, *68*, 3503−3505.
(51) Friedrich, S. Superconducting Tunnel Junction Photon Detectors: Theory and Applications. *J. Low Temp. Phys.* **2008**, *151*, 277−286.
(52) Ohkubo, M. Superconducting Detectors for Particles from Atoms to Proteins. *Phys. C* **2008**, *468*, 1987−1991.
(53) Aksenov, A. A.; Bier, M. E. The Analysis of Polystyrene and Polystyrene Aggregates into the Mega Dalton Mass Range by Cryodetection MALDI TOF MS. *J. Am. Soc. Mass Spectrom.* **2008**, *19*, 219−230.
(54) Wenzel, R. J.; Matter, U.; Schultheis, L.; Zenobi, R. Analysis of Megadalton Ions Using Cryodetection MALDI Time-of-Flight Mass Spectrometry. *Anal. Chem.* **2005**, *77*, 4329−4337.
(55) Yanes, O.; Avilés, F. X.; Wenzel, R.; Nazabal, A.; Zenobi, R.; Calvete, J. J. Proteomic Profiling of a Snake Venom Using High Mass Detection MALDI-TOF Mass Spectrometry. *J. Am. Soc. Mass Spectrom.* **2007**, *18*, 600−606.
(56) Plath, L. D.; Ozdemir, A.; Aksenov, A. A.; Bier, M. E. Determination of Iron Content and Dispersity of Intact Ferritin by Superconducting Tunnel Junction Cryodetection Mass Spectrometry. *Anal. Chem.* **2015**, *87*, 8985−8993.
(57) Plath, L. D.; Wang, Z.; Yan, J.; Matyjaszewski, K.; Bier, M. E. Characterization of ZnO Nanoparticles Using Superconducting Tunnel Junction Cryodetection Mass Spectrometry. *J. Am. Soc. Mass Spectrom.* **2017**, *28*, 1160−1165.
(58) Sipe, D. M.; Ozdemir, A.; Firek, B. A.; Hendrix, R. W.; Bier, M. E. Analysis of Viral Capsid HK97 *via* Cryodetection MALDI TOF in the MegaDalton Mass Range. In *Proceedings of the 56th ASMS Conference on Mass Spectrometry and Allied Topics*; Denver, CO, USA, June 1−5, 2008.
(59) Watt, A. A. R.; Blake, D.; Warner, J. H.; Thomsen, E. A.; Tavenner, E. L.; Rubinsztein-Dunlop, H.; Meredith, P. Lead Sulfide Nanocrystal: Conducting Polymer Solar Cells. *J. Phys. D: Appl. Phys.* **2005**, *38*, 2006−2012.
(60) Dale, M. J.; Dyson, P. J.; Johnson, B. F. G.; Langridge-Smith, P. R. R.; Yates, H. T. Laser-Desorption Mass Spectrometry of $[Ru_6C(CO)_{17}]$ and Its Derivatives: Cluster Aggregation in the Gas Phase. *J. Chem. Soc., Dalton Trans.* **1996**, 771−774.
(61) Leach, K. Personal communication, 2007.
(62) Spengler, B. Post-Source Decay Analysis in Matrix-Assisted Laser Desorption/Ionization Mass Spectrometry of Biomolecules. *J. Mass Spectrom.* **1997**, *32*, 1019−1036.
(63) Chaki, N. K.; Negishi, Y.; Tsunoyama, H.; Shichibu, Y.; Tsukuda, T. Ubiquitous 8 and 29 kDa Gold:Alkanethiolate Cluster Compounds: Mass-Spectrometric Determination of Molecular Formulas and Structural Implications. *J. Am. Chem. Soc.* **2008**, *130*, 8608−8610.
(64) Whetten, R. L.; Khoury, J. T.; Alvarez, M. M.; Murthy, S.; Vezmar, I.; Wang, Z. L.; Stephens, P. W.; Cleveland, C. L.; Luedtke,

DOI: 10.1021/acsnano.7b08541
ACS Nano 2018, 12, 2591−2602

W. D.; Landman, U. Nanocrystal Gold Molecules. *Adv. Mater.* **1996**, *8*, 428−433.
(65) Schaaff, T. G.; Shafigullin, M. N.; Khoury, J. T.; Vezmar, I.; Whetten, R. L.; Cullen, W. G.; First, P. N.; Gutiérrez-Wing, C.; Ascensio, J.; Jose-Yacamán, M. J. Isolation of Smaller Nanocrystal Au Molecules: Robust Quantum Effects in Optical Spectra. *J. Phys. Chem. B* **1997**, *101*, 7885−7891.
(66) Tsunoyama, H.; Negishi, Y.; Tsukuda, T. Chromatographic Isolation of "Missing" Au_{55} Clusters Protected by Alkanethiolates. *J. Am. Chem. Soc.* **2006**, *128*, 6036−6037.
(67) Bruchez, M. P.; Moronne, M.; Gin, P.; Weiss, S.; Alivisatos, A. P. Semiconductor Nanocrystals as Fluorescent Biological Labels. *Science* **1998**, *281*, 2013−2016.
(68) Chan, W. C. W.; Nie, S. Quantum Dot Bioconjugates for Ultrasensitive Nonisotopic Detection. *Science* **1998**, *281*, 2016−2018.
(69) Parak, W. J.; Gerion, D.; Zanchet, D.; Woerz, A. S.; Pellegrino, T.; Micheel, C.; Williams, S. C.; Seitz, M.; Bruehl, R. E.; Bryant, Z.; Bustamante, C.; Bertozzi, C. R.; Alivisatos, A. P. Conjugation of DNA to Silanized Colloidal Semiconductor Nanocrystalline Quantum Dots. *Chem. Mater.* **2002**, *14*, 2113−2119.
(70) Derfus, A. M.; Chan, W. C. W.; Bhatia, S. N. Probing the Cytotoxicity of Semiconductor Quantum Dots. *Nano Lett.* **2004**, *4*, 11−18.
(71) Hoshino, A.; Fujioka, K.; Oku, T.; Suga, M.; Sasaki, Y. F.; Ohta, T.; Yasuhara, M.; Suzuki, K.; Yamamoto, K. Physicochemical Properties and Cellular Toxicity of Nanocrystal Quantum Dots Depend on Their Surface Modification. *Nano Lett.* **2004**, *4*, 2163−2169.
(72) Quaroni, L.; Chumanov, G. Preparation of Polymer-Coated Functionalized Silver Nanoparticles. *J. Am. Chem. Soc.* **1999**, *121*, 10642−10643.
(73) Zhang, F.; Lees, E.; Amin, F.; RiveraGil, P.; Yang, F.; Mulvaney, P.; Parak, W. J. Polymer-Coated Nanoparticles: A Universal Tool for Biolabelling Experiments. *Small* **2011**, *7*, 3113−3127.
(74) Jokerst, J. V.; Lobovkina, T.; Zare, R. N.; Gambhir, S. S. Nanoparticle PEGylation for Imaging and Therapy. *Nanomedicine* **2011**, *6*, 715−728.
(75) Chakraborty, S. K.; Fitzpatrick, J. A. J.; Phillippi, J. A.; Andreko, S.; Waggoner, A. S.; Bruchez, M. P.; Ballou, B. Cholera Toxin B Conjugated Quantum Dots for Live Cell Labeling. *Nano Lett.* **2007**, *7*, 2618−2626.
(76) Andreko, S. Personal communication, 2007.

DOI: 10.1021/acsnano.7b08541
ACS Nano 2018, 12, 2591−2602